JGR Solid Earth

RESEARCH ARTICLE
10.1029/2021JB023540

A New Probe Into the Innermost Inner Core Anisotropy via the Global Coda-Correlation Wavefield

Thuany Costa de Lima[1], Hrvoje Tkalčić[1], and Lauren Waszek[2,3]

[1]Research School of Earth Sciences, The Australian National University, Canberra, ACT, Australia, [2]Physical Sciences, James Cook University, Douglas, QLD, Australia, [3]Department of Physics, New Mexico State University, Las Cruces, NM, USA

Key Points:

- We develop a novel method based on the correlation wavefield and we confirm a distinct anisotropic structure in the innermost inner core
- Our study is based on the correlation feature I2* and is independent of seismological tools used in the direct seismic wavefield
- We model a cylindrically-anisotropic innermost inner core with 3.3% strength and slow direction at ∼55° from the Earth's rotation axis

Supporting Information:

Supporting Information may be found in the online version of this article.

Correspondence to:

T. Costa de Lima,
Thuany.CostadeLima@anu.edu.au

Citation:

Costa de Lima, T., Tkalčić, H., & Waszek, L. (2022). A new probe into the innermost inner core anisotropy via the global coda-correlation wavefield. *Journal of Geophysical Research: Solid Earth*, *127*, e2021JB023540. https://doi.org/10.1029/2021JB023540

Received 2 NOV 2021
Accepted 14 MAR 2022

Abstract Investigations of the Earth's inner core (IC) using seismic body waves are limited by their volumetric sampling due to uneven global distribution of large earthquakes and receivers. The sparse coverage of the IC leads to uncertainties in its anisotropy, the directional dependence of seismic velocity. Yet, detailed constraints on anisotropy, such as its magnitude, and spatial distribution, are required to understand the crystallographic structure of IC's iron and its solidification and deformation processes. Here, we present a new method to investigate the IC's anisotropic properties based on Earth's coda-correlation wavefield constructed from the late coda of large earthquakes. We perform a comprehensive travel time analysis of I2*, an IC-sensitive correlation feature identified as a counterpart of the direct seismic wavefield's PKIKPPKIKP waves, yet fundamentally different. Namely, I2* is a mathematical manifestation of similarity among specific seismic phases with the same slowness detected in global correlograms in the short inter-receiver distance range. Our new spatial sampling of the IC overcomes the shortage of direct seismic wavefield paths sensitive to the IC's central volume, also known as the innermost IC (IMIC). The observed I2*'s travel time variations relative to Earth's rotation axis (ERA) support a model of cylindrical anisotropy with 3.3% strength and a zonal pattern of slow axis oriented 55° from ERA. We thus find compelling evidence for a deep IC structure with distinct anisotropy, although we cannot resolve the depth at which the change occurs. This finding reinforces previous inference on the IMIC, with implications for Earth's evolution.

Plain Language Summary Cylindrical anisotropy, a type of transverse isotropy, was hypothesized to exist in the inner core (IC) to explain the directional dependence of travel times of compressional (PKIKP) waves propagating through it. Namely, PKIKP waves aligned with the Earth's rotation axis (ERA) were noticed to arrive earlier than those traveling in the equatorial direction. Anisotropy is essential to determine the crystallographic structure of iron in the IC, and it holds the key to understanding its growth and evolutionary processes. However, anisotropy's strength and radial dependency to date remain partly constrained by existing seismological methods and data, and a simple conceptual model put forward initially has been challenged multiple times. We demonstrate the feasibility of constraining the IC anisotropy with global correlation stacks of the late-coda seismic wavefield generated by reverberations in the Earth many hours after large earthquakes. The newly developed method to measure the seismic properties of the innermost IC (IMIC) via an optimal configuration of podal and antipodal sources and receivers provides a unique sampling of previously inaccessible IC volumes. Our results confirm the IMIC is characterized by a different anisotropy than the bulk IC, with the slow direction of anisotropy directed ∼55° from the ERA and 3.3% strength.

1. Introduction and Motivation

1.1. Inner Core Anisotropy

The Earth's inner core (IC) is a solid ball with a radius of about 1,220 km (e.g., Kennett et al., 1995) located in the center of our planet. As the Earth cools, the IC grows over time through solidification of the liquid outer core (Buffett et al., 1992; Jacobs, 1953). The release of latent heat and light elements during solidification drives convection in the outer core, providing energy for the geodynamo and generating Earth's magnetic field (e.g., Gubbins et al., 2003; Labrosse & Macouin, 2003; Loper, 1984). In addition to the decay of radioactive isotopes and the Earth's long-term secular cooling, the heat loss from the Earth's core is one of the largest energy sources driving the mantle convection—the primary mechanism responsible for plate tectonics. Therefore, studies on the IC have the potential to unravel the history of the internal dynamic processes of our planet. Unfortunately, progress on seismic imaging of the Earth's IC is limited by the poor worldwide distribution of large sources and

seismic receivers; significant earthquakes are dominantly confined to the equatorial belt subduction zones, and seismic stations are deployed unevenly around the world. Advances in data processing techniques and new methods are required to place improved constraints on its structure.

Since its discovery in 1936 (Lehmann, 1936), the IC has remained one of the most challenging parts of the Earth's interior to be investigated (Tkalčić, 2017). This is because much of what is known about its structure originates from seismological studies of two main data types: seismic body waves and Earth's normal modes or free oscillations. The first evidence of heterogeneity in the Earth's IC was found by Poupinet et al. (1983), who observed a shorter P-wave travel time in the polar direction than the equatorial. The concept of seismic anisotropy was subsequently proposed to explain the observation of compressional waves propagating through the IC faster in quasi-polar directions (Morelli et al., 1986) and anomalous splitting of core-sensitive free oscillations (Woodhouse et al., 1986).

Anisotropy in the IC is linked to the crystal organization of iron-nickel alloy at high pressure (e.g., Bergman, 1997; Bergman et al., 2018; Jeanloz & Wenk, 1988; Karato, 1993, 1999; Yoshida et al., 1996), which is the core's main mineral constituent. Hence, details of anisotropic properties inform regarding the IC growth and texturing processes over time. The preferred orientation of different iron phases (mostly hexagonal-closed-packed (hcp) and body-centered-cubic (bcc) iron crystals) have been proposed to explain the origin of anisotropy in the IC. However, the difficulty in computing the elastic properties of these iron phases at core pressure and temperature conditions results in debates for which iron phase best matches the seismological observations (e.g., Belonoshko et al., 2008; Jackson et al., 2000; Li et al., 2018; Mattesini et al., 2018; Ritterbex & Tsuchiya, 2020; Romanowicz et al., 2016; Stixrude & Cohen, 1995).

The increase of the anisotropy strength in the innermost 300 km of the IC was initially found by Su and Dziewonski (1995). An innermost inner core (IMIC) with distinct anisotropy from the bulk IC was hypothesized to explain the pattern of travel time residuals at antipodal epicenter distances (Ishii & Dziewoński, 2002). Based on an analysis of PKIKP phases bottoming at different depths, Ishii and Dziewoński (2003) suggested that the IMIC can be modeled with a ball of a 300 km radius and the fast axis of anisotropy tilted from the ERA with 3.7% of strength. In their model, the slow axis of anisotropy in the IMIC is at an angle of 45° from the ERA, as opposed to the OIC's slow axis of anisotropy pronounced in the equatorial direction. A follow-up study based on splitting of normal modes (Beghein & Trampert, 2003) confirmed the IMIC with a radius of ∼400 km, compatible with none of the hcp iron models, thereby suggesting a phase of iron in the IMIC different from hcp.

Subsequent investigations using different datasets and methods led to a variety of IMIC anisotropy models that are inconsistent in several aspects, such as the strength of its anisotropy (from nearly isotropic up to 6%), IMIC boundary radius (ranging from 300 to 820 km), the slow and fast propagation directions (e.g., Calvet et al., 2006; Cao & Romanowicz, 2007; Cormier & Stroujkova, 2005; Niu & Chen, 2008, Romanowicz et al., 2016; Stephenson et al., 2020; Vinnik et al., 1994; T. Wang et al., 2015). Each proposed IC anisotropy model (with or without IMIC) has different implications for IC formation and its evolution. Hence, further investigation is critical to understand and reconcile the inconsistencies between the models. Travel time analysis of high-frequency body-waves is typically performed to examine the fine structure of the IC. However, seismic coverage of high-quality data sensitive to the IMIC is insufficient to constrain IC physical properties further. Therefore, the exact nature of anisotropy is yet to be determined, and new methods must augment traditional seismological tools. One of the promising new tools is the exploration of the earthquake coda-correlation wavefield.

1.2. Coda-Correlation Wavefield

The cross-correlation of seismograms has emerged as a powerful tool to image the structure of the Earth's subsurface through the exploitation of diffusive regime of surface waves (e.g., Campillo & Paul, 2003; Ruigrok et al., 2008; Wapenaar & Fokkema, 2006; Wapenaar et al., 2010). Multiple studies have applied the concept of interferometry to ambient noise records to investigate the structure of the crust, mantle transition zone, and the lowermost mantle using dense arrays of receivers (e.g., Feng et al., 2017; Poli et al., 2012; Retailleau et al., 2020; Sabra et al., 2005; Shapiro & Campillo, 2004; Zhan et al., 2010). The global coda correlograms are obtained by stacking the cross-correlation functions of the coda of large events sorted in time and the angular-distance bins between receiver pairs (Figure 1a). The early understanding of how the features observed in global correlograms are formed led to extending the concept of interferometry from records of ambient noise to the coda of large

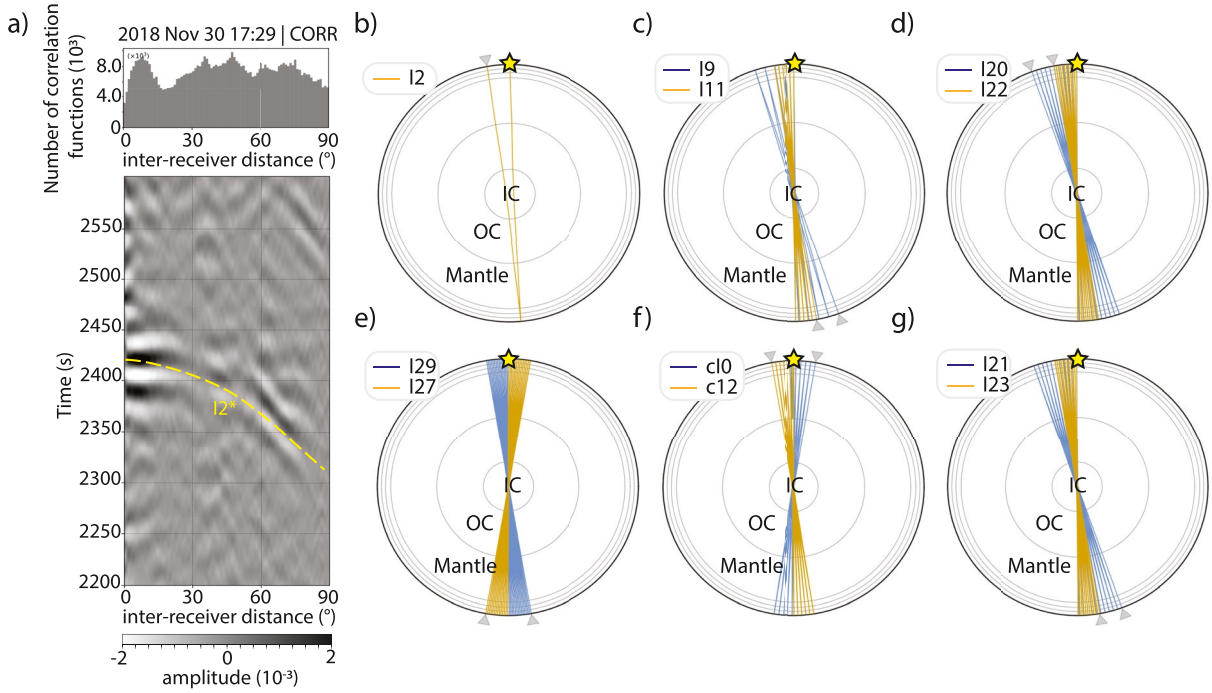

Figure 1. Formation mechanism of I2*. (a) Coda-correlogram calculated using recordings of the 30 November 2018, M_w = 8.2, Alaska, earthquake. Yellow dashed line represents the travel time of I2* predicted using ak135 (Kennett et al., 1995); (b) raypath of I2 (PKIKPPKIKP) at the referent epicenter distance of 10°; (c–g) Examples of I2* formation at a short inter-receiver distance from multiple correlation-feature constituents for different geometries of sources and receivers.

earthquakes (i.e., hours of records after a seismic event), with applications to the core-mantle boundary and IC (e.g., Boué et al., 2013, 2014; Huang et al., 2015; Lin & Tsai, 2013; Poli et al., 2015; T. Wang et al., 2015; Wu et al., 2018; Xia et al., 2016).

Recently, Phạm et al. (2018) and Tkalčić and Phạm (2018) proposed and exploited a physical mechanism responsible for generating features observed in the cross-correlation stacks including the non-causal "body-wave-like" arrivals (e.g., Boué et al., 2014; Ruigrok et al., 2008; Snieder et al., 2006) and the anomalous amplitudes on both synthetic and observed cross-correlograms (e.g., Boué et al., 2014; Lin & Tsai, 2013; Poli et al., 2017). Within the ray theory, the non-causal features can be explained by the interference among seismic phases with the same ray parameter, but only with a subset of propagation legs in common. Kennett and Phạm (2018a) used the generalized-rays formalism to corroborate the point on the same slowness, and S. Wang and Tkalčić (2020a) demonstrated that the correlogram features are indeed composed of the reverberating constituents. At the time it was proposed, this formation mechanism was inconsistent with the above-mentioned early understanding and the common belief that the body-wave part of the Green's function is reconstructed, but aligned with the idea that high-quality normal modes might be responsible (Poli et al., 2017). In summary, the correlation wavefield theory accounts for all correlation features that emerge in the global cross-correlation stacks (for a recent review, see Tkalčić et al., 2020).

More recently, S. Wang and Tkalčić (2020a, 2020b) proposed a new framework for coda-correlation tomography using an approach in which the correlation features' constituents are used to build the sensitivity kernels for the IC tomography. Their study quantitatively describes the relationship between the coda-correlation wavefield and the Earth structure, using a particular correlation feature sensitive to the IC: I2* (Figure 1). The asterisk is used to distinguish this feature from its counterpart in the seismic wavefield: I2 (a.k.a. PKIKPPKIKP; see Tkalčić et al. (2020) for a detailed description of the correlation field nomenclature). In this study, we develop a new method to probe the IMIC anisotropy based on the timing of the correlation feature I2*. The constituents of I2* are sensitive to the IC's center, which is poorly explored by antipodal PKP ray paths. We first propose and describe the new methodology. Subsequently, we analyze the I2* travel time observations to investigate the IC P-wave velocity anisotropy independently from the direct seismic wavefield. We then describe our findings,

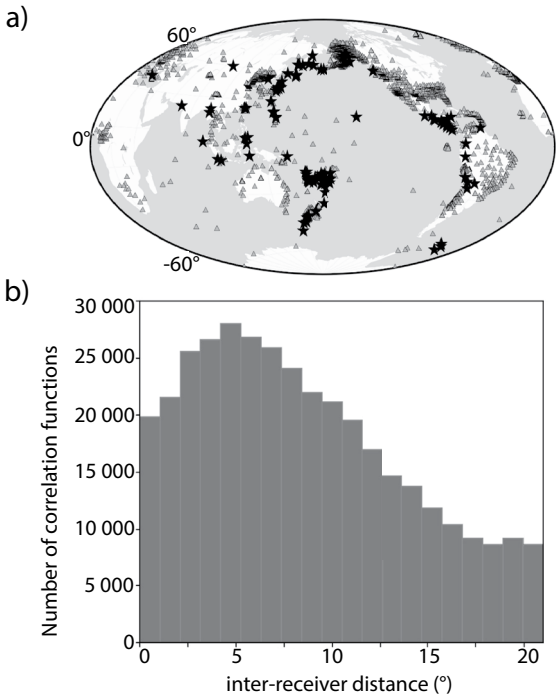

Figure 2. (a) Global distribution of stations (triangles) and 105 events (stars) used in this study. (b) Histogram of station pairs (correlation functions) for the 105 events with the inter-receiver distances binned in 1°.

most importantly, evidence for a distinct anisotropy in the IMIC, aligned with recent results from body-wave observations. We discuss our results and future work in the context of existing knowledge of the IC.

2. New Method Development

2.1. Correlation Feature I2* and Its Formation Mechanism

Among the correlation features observed in the global correlograms, we select I2* to probe the anisotropic structure of the IC. In a recently published catalog of the correlation features, I2* is particularly prominent (Tkalčić & Phạm, 2020). I2* is identified easily in nearly podal station pairs (i.e., small inter-receiver distances) of stacked correlation functions, and its constituents sample the IC's center multiple times. I2* is equally prominent as I* (counterpart of PKIKP in the seismic wavefield) or even exceeds I*'s strength because it is formed by cross-correlating seismograms recorded on seismic stations in proximity. Many more such station pairs are globally distributed than those at antipodal distances (Figure S1 in Supporting Information S1). For a complete description of correlogram formation, we refer the reader to Tkalčić et al. (2020).

The counterpart of I2* in the seismic wavefield is the podal PKIKPPKIKP (a.k.a. P'P'df or sometimes, I2; Figure 1), which is rarely observed (e.g., Tkalčić et al., 2006). Despite the similarities in travel time and slowness between these two data types, I2* and I2 are fundamentally different (Figure 1). The formation of I2* can be understood intuitively as the result of differential travel times between any pair of seismic phases with the time difference equivalent to the I2's travel time. For instance, I6–I4, I9–I7, I12–I10, PcPI2–PcP, etc., can all produce a peak in the correlation function with travel times similar but not exactly equal to the I2 seismic phase (Tkalčić et al., 2020; S. Wang & Tkalčić, 2020a, 2020b). Although a large number of possible combinations can arise from the late coda, the contribution of cross-terms with a high number of reverberations (e.g., PcPPcPI4–PcPPcPI2) is less significant than those with fewer reverberations (e.g., I4–I2) due to the attenuation effect (S. Wang & Tkalčić, 2020a, 2020b).

2.2. Data Processing and I2* Feature Selection From the Global Correlogram

We process records of earthquakes with Mw ≥ 6.8 at all depths listed in the global centroid moment tensor catalog (Ekström et al., 2012) from 1999 to 2019 (Figure 2). The seismograms recorded by broadband receivers of permanent and temporary networks were downloaded from the Incorporated Research Institutions for Seismology Data Management Center (IRIS DMC). The data processing follows the steps described in Tkalčić et al. (2020).

After downloading the vertical component seismograms, we systematically remove the mean, linear trends, correct the instrumental response, and resample the waveforms at a rate of 0.1 s. The waveforms are normalized twice to suppress energy derived from the earthquake and aftershocks. The first normalization is calculated in the time domain by the running-absolute-mean method (the details of the temporal normalization are described in Bensen et al., 2008). Subsequently, to reduce the contributions of any dominant frequency, we apply the Fourier transform and normalize the complex spectrum of the waveforms using a spectral whitening operation (Phạm & Tkalčić, 2018).

The cross-correlation is then computed in the frequency domain, and an inverse Fourier Transform converts the traces back to the time domain. The waveform is folded in time 0, and the positive lag time is retained. Previous studies (e.g., Lin & Tsai, 2013; Phạm et al., 2018; Xia et al., 2016) show that the correlation features for the periods between 15 and 50 s arise from the energy recorded within the time window of 10,000–35,000 s (~3–10 h) after their origin time. After the cross-correlations functions are calculated, the waveforms are linearly stacked in bins of inter-receiver distances and then filtered at an intermediate frequency band of 15–50 s.

We select a subset of 105 events with high-quality I2* waveforms (Table S1 in Supporting Information S1). Most of these earthquakes are generated by normal and reverse focal mechanisms of short source-time function duration—shown to produce high-quality global coda-correlograms due to favorable energy radiation (Tkalčić & Phạm, 2020). In fact, only 10 of these events were used recently to produce a new spherically symmetric model of the Earth (Ma & Tkalčić, 2021). The epicentral distance of earthquakes relative to each receiver pair is selected based on the stationary principle and the details are described in Sections 2.4 and 2.5. Finally, we use the I2* waveform coherency as a quality criterion. Cross-correlation functions of records in the inter-receiver distance range between 4° and 9° show higher similarity and smaller variations in the timings of I2* when compared to other inter-receiver distance ranges (Figure S2 in Supporting Information S1). Consequently, we use the stacks of waveforms binned only at those inter-receiver distances to model the anisotropy.

2.3. Definition of ξ^*

During the late-coda time window of 3–10 h after the event origin time, the theoretical PKIKP reverberates from nine to 30 times through the IC. Thus, the formation of I2* results from the similarity of seismic phases that reverberate at least nine times within the IC given the cross-correlation of seismic records is based on the podal-antipodal source-receiver geometry. For each receiver pair, we represent the sampling direction of I2* in the IC as the same as a PKIKP raypath traveling steeply through its center and with a point of intersection with the Earth's surface at longitude θ and colatitude ξ^*. Such definition of I2* raypath is a good approximation for the kernel of I2* because the most dominant cross-terms contributing to its generation stem from steeply traveling body waves such as I12–I10, I13–I11, and higher multiples (Kennett and Phạm, 2018b; S. Wang & Tkalčić, 2020a). More specifically, we define the colatitude ξ^* (the angle between I2* raypath in the IC and the ERA) as:

$$\cos \xi^* = \frac{\boldsymbol{L} \cdot \boldsymbol{K}}{|\boldsymbol{L}|\,|\boldsymbol{K}|} \tag{1}$$

where $\boldsymbol{L}$ is the vector representing the direction of I2 in the IC propagating from the receiver R1 to the receiver R2. The unit vector $\boldsymbol{K}$ represents the direction parallel to the ERA. The definitions of vectors $\boldsymbol{L}$ and $\boldsymbol{K}$ are the same as described in Tkalčić (2017), with the only difference that, here, vector $\boldsymbol{L}$ is the average direction between the PKIKP legs of I2 and the ERA at short angular distances between receivers ($\leq 9°$).

2.4. Testing the Sensitivity of I2* to IC Anisotropy

We explore the sensitivity of the timing of I2* to changes in P-wave velocity in the IC, and investigate the azimuthal variations of the source relative to the anisotropy's fast axis. Synthetic waveforms are produced using the axisymmetric spectral element method, AxiSEM v.1.3 (Nissen-Meyer et al., 2014). Due to computational expenses, the sources considered in the numerical simulation are relatively simple—explosive sources. We use a computational mesh of 5 s with stations distributed every 0.1° along a great-circle plane intersecting the north pole. After generating 10-h records of the synthetic seismograms, the processing steps to compute the synthetic correlogram are the same as those for the actual data (for details, refer to Section 2.5).

To simulate IC anisotropy with a fast axis parallel to ERA, we use ak135 (Kennett et al., 1995) as a background model and compare it to ak135 with an increased IC υ_p of 3.2% along the polar direction (Van Driel & Nissen-Meyer, 2014), which is a similar strength of IC anisotropy inferred by pioneering studies (e.g., Morelli et al., 1986; Tromp, 1993). The negative peak in the amplitude (white fringe) at 2,405 s on the correlogram (Figure 3a) followed by a positive peak in the amplitude (black fringe) corresponds to the energy arrival of I2*. For a source located at the equator and a fast axis of propagation parallel to the ERA, the travel time of I2* detected in the correlogram is similar to the travel time of I2* estimated using the 1D-isotropic υ_p IC model (Figure 3b). However, with the source located at the north pole (Figure 3c), we observe a 13 s earlier arrival time of I2* compared to cases of both isotropic IC (Figure 3b) and anisotropic IC with the source at the equator (Figure 3a). This 13 s difference is the time predicted for a P-wave propagating twice along the fast axis of anisotropy in the IC with a 3.2% υ_p increase. Hence, the numerical simulation demonstrates that I2*'s travel times are sensitive to υ_p anisotropy in the IC, validating our proposed method. Furthermore, this synthetic experiment illustrates the dependency of the time observations on the earthquake location.

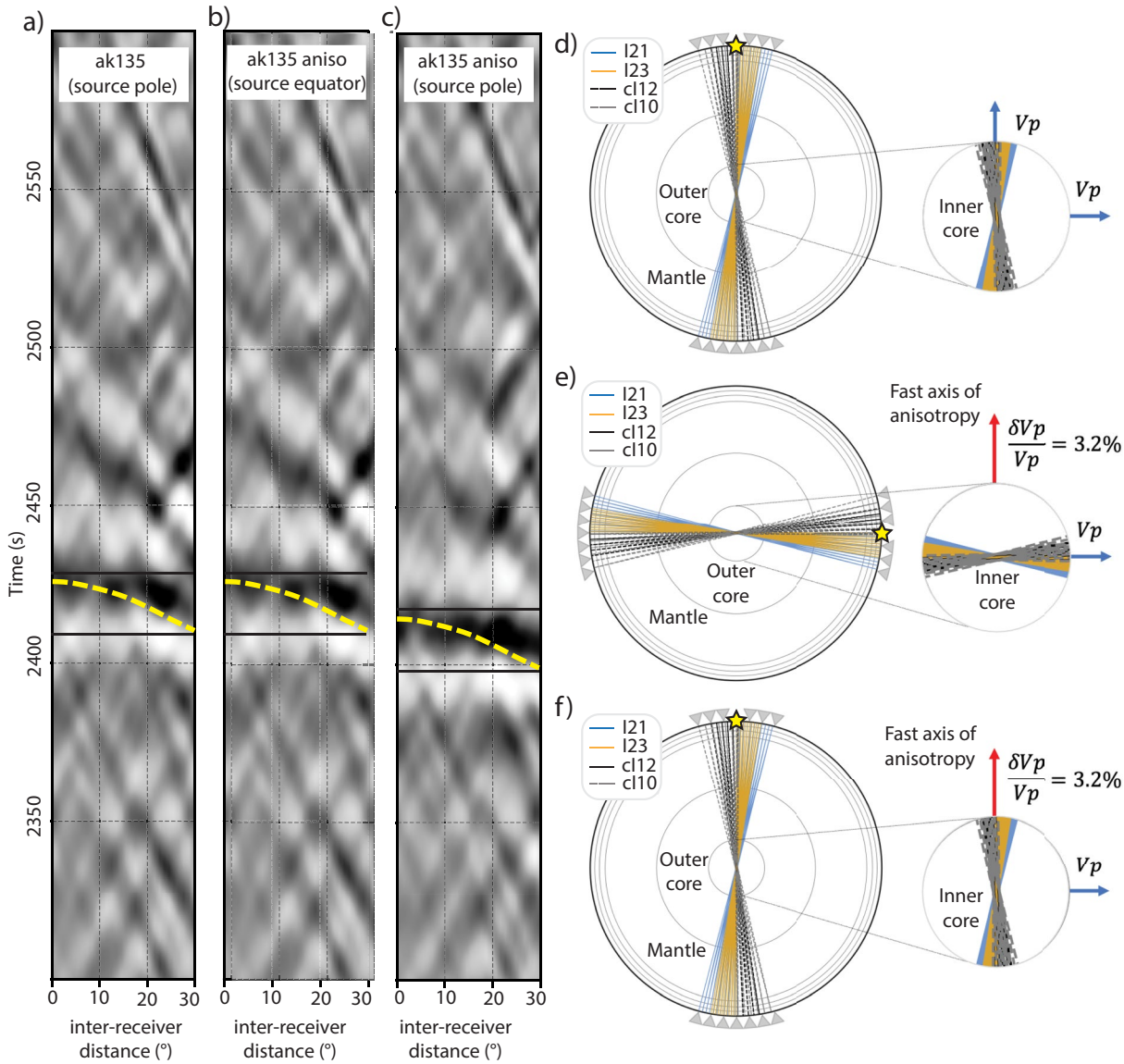

Figure 3. Comparison of synthetic correlograms calculated using isotropic and anisotropic IC models and varying source-receiver geometry, and graphical representation of the I2* constituents raypaths. (a) Correlogram calculated using the spherically symmetric model ak135 (Kennett et al., 1995); (b) correlogram calculated using an anisotropic model of IC and an explosive source located at the equator (c) same as (b) but with an explosive source located at the north pole. For reference, the dashed yellow lines in (a and b) indicate the theoretical times of I2 seismic phase predicted using ak135; the dashed yellow line in (c) is the predicted I2 arrival time for ak135 with 3.2% anisotropy; (d–f) illustrate seismic ray constituents contributing to the formation of I2* for each configuration of source, receivers, and P-wave velocity used to estimate the correlograms in (a–c), respectively. The red arrows indicate the direction of the fast axis of cylindrical anisotropy in the IC with a strength of 3.2% (indicated by the blue arrows). Note that the correlograms in (a and b) are identical, whereas I2* (centered on the positive peak of correlation represented by the black fringe) arrives earlier by approximately 13 s in (c).

Due to the constituents of I2* sampling the IC volume through its center, the travel times of I2* are integrations over the bulk IC, including the innermost IC. We demonstrate the sensitivity of I2* to the innermost 600 km radius of the IC via an additional synthetic test (Figure S3 in Supporting Information S1), proving that the travel times of I2* depend on the velocity of compressional waves in the first 600 km radius of the IC.

2.5. Podal-Antipodal Receiver Stacking

In addition to the location of the source, the angular distance between receivers and their distances from the events also influence the I2* timing. I2* is generated by contributions of multiple cross-terms that sample the IC

exhibiting complex geometries and mixed directions (S. Wang & Tkalčić, 2020a), thus leading to an observed travel time that is an average of raypaths propagating along multiple orientations. Here, we constrain the direction of propagation of I2* cross-terms by selecting receiver pairs of inter-receiver distance ≤9°, located nearly podal (defined as $\Delta \leq 20°$) and antipodal (defined as $\Delta \geq 160°$) to each earthquake; hence, the events and receivers are grouped similarly to geographical spherical bins of 10° radius. The stacks of cross-correlation functions calculated using this optimal geometry of source-receiver pairs are hereafter called the podal-antipodal receiver stacks. We calculate these stacks for individual earthquakes. This means that the records from station pairs near or antipodal to an event are cross-correlated with each other and then those correlograms are stacked. Thus, the formation of I2* associated with each event results from constituents traveling steeply through the central part of the IC. A notable difference in the timing of I2* calculated with the careful selection of podal-antipodal source-receivers stacks and without it can be observed in Figure S4 of Supporting Information S1.

2.6. IC Anisotropy Measurements and Corrections for Earth's Ellipticity and Mantle Heterogeneities

Conventionally, IC anisotropy is estimated by analyzing directional dependence in the travel times of raypaths propagating at different directions and depths in the IC (e.g., Creager, 1992; Souriau & Romanowicz, 1996; Vinnik et al., 1994). The direction of propagation is typically defined by an angle ξ between the PKIKP ray path in the IC and the ERA. Here, we analyze the directional dependence of I2* correlogram times on the angle ξ* using the podal-antipodal receiver stacks. Then, we present our observations in two different ways: (1) the correlogram times of I2* as a function of ξ* of the raypaths (Figure 4), and (2) the correlogram times of I2* as a function of both longitude θ and the angle ξ* of the raypaths (Figure 5). In the latter, the cross-correlation functions are stacked within geographical bins of 10° (latitudinally) × 45° (longitudinally) because individual cross-correlation functions are noisy. Thus, the cross-correlation functions calculated from records of inter-receiver distances from 4° to 9° are summed together to enhance the signal-to-noise ratio of I2* (Figure 6). We discard bins that are sampled by fewer than 100 raypaths since we find that only stacks of at least 100 waveforms show a clear arrival of I2*. After linearly stacking the cross-correlations functions into bins, we end up with 21 stacked waveforms of high-quality I2* (Figure 6) which are used for the modeling. Prior to stacking, we do not align the waveforms on the arrivals of I2* because the move-out effect is expected to be equal amongst all bins (as we average the times), and not influence the relative measurements of I2*. Finally, we use cross-correlation to measure the delay time between the stacked waveform of each bin and a reference waveform, obtained as the stack of cross-correlation functions (from 4° to 9° of interstation distances) of correlogram ‘‘g’’ in Figure 4, sensitive to equatorial paths only.

In order to study the data trend caused by the IC anisotropy, we must remove contributions to the travel times by Earth's ellipticity and 3D mantle heterogeneity. Due to the computational expenses in estimating the ellipticity correction for all possible constituents of each I2*, we apply the Earth's ellipticity corrections similarly to correcting regular seismic phases (Kennett & Gudmundsson, 1996). We first calculate the raypaths of the seismic phase I2 propagating between each receiver pair. The time correction for ellipticity is estimated for both legs of PKIKP: the first one travels from a receiver in Point A through the IC, reflecting from the Earth's surface, and the second one travels back through the IC to Point B (the other receiver).

We correct travel times for 3D mantle heterogeneities by estimating the cumulative travel time of an I2 wave traveling steeply four times through the mantle: twice on the podal side, and twice on the antipodal side. For each leg, we calculate mantle delay times for every 50 km depth from Earth's surface to the core-mantle boundary, using the recent DETOX-P3 tomography model (Hosseini et al., 2020). In order to account for the size of the I2* Fresnel zone, we calculate average delay times for a cylinder of 10° lateral radius around each mantle ray path. This radius is chosen because it corresponds to the size of our spherical bins, and is equivalent to the distance between the receiver-pairs we use in this study—reasonable for a long period nature of I2* (Figure S5 in Supporting Information S1). We then sum across the four mantle legs to obtain the total mantle correction. Corrections via ray-tracing for different models of mantle heterogeneities do not vary significantly (Table S2 in Supporting Information S1). Since our data travel through the IC approximately as a PKIKP raypath at 180° epicentral distance, I2* travel-time observations are only dependent on the radial variations of heterogeneities in the mantle or ICB.

The ellipticity and mantle-corrected travel-time residuals of I2*, t_{I2*}, are then obtained by

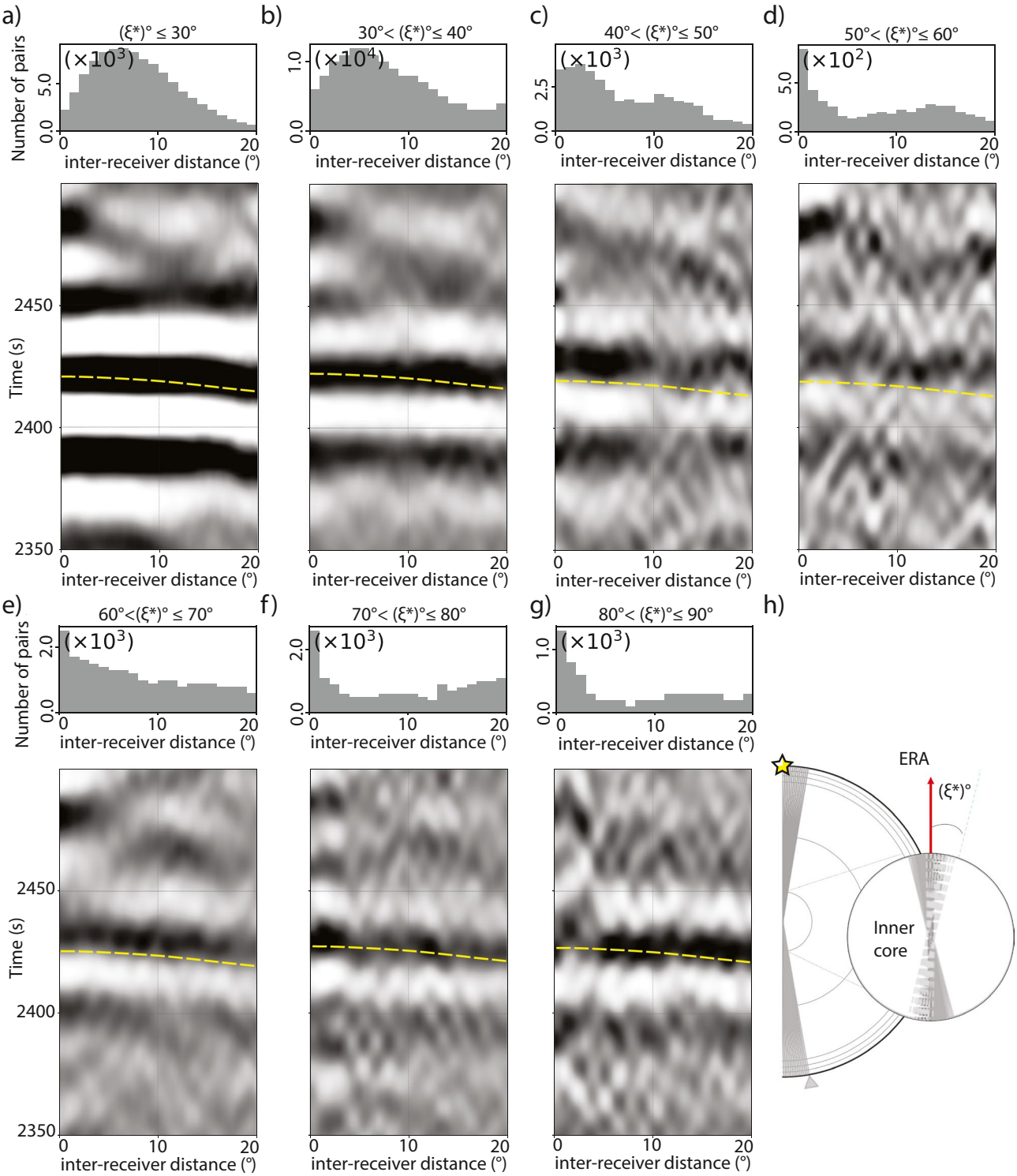

Figure 4. The stacked correlograms for 1° binned inter-receiver distance calculated from the waveforms of 105 earthquakes, and graphical representation of the angle ξ^* between the ERA and I2* raypaths. (a–g) Podal-antipodal receiver stack correlograms focusing on I2* for different angles of I2* kernel in the IC with respect to ERA. Panels on top of each correlogram are histograms of all station pairs on the global scale with inter-receiver distance binned in 1°. The time range displayed from 2,350 to 2,500 s. The angle ξ^* of the waveforms used to calculate the correlograms is indicated on the top of the histograms. For reference, the prediction of the seismic phase I2 (corrected for the Earth's ellipticity) is plotted by yellow dashed lines. Note the variation in the arrival time of I2* for different ξ^*: in the black fringe near 2,425 s arrives earlier relative to I2 predictions for raypaths traveling near to polar and equatorial directions, panels (a and g), respectively. (h) The geometry of I2* constituents traveling in the IC along ERA (red arrow) used to calculate correlogram in (a).

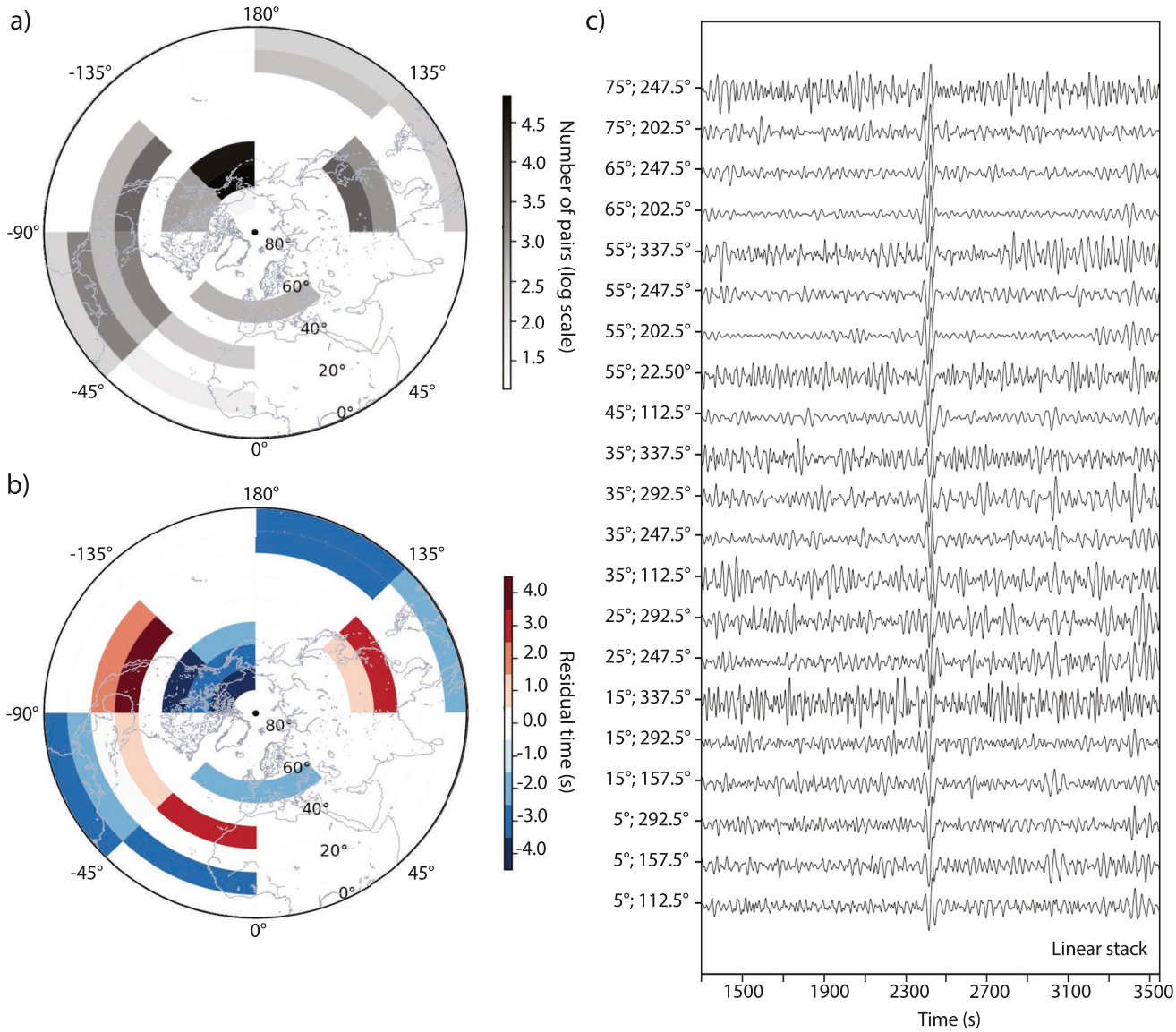

Figure 5. Distribution of I2* binned into 72 spatial bins delineated latitudinally and longitudinally (see the main text for more detail) and I2* linear stacks. (a) The number of cross-correlation functions within each bin on a logarithmic scale. Unsampled bins or bins sampled by waveforms of low quality are left uncolored. (b) Travel time difference of the observed I2* from the theoretically predicted times. The times of the I2* constituents are corrected for the Earth's ellipticity (Kennett & Gudmundsson, 1996) and mantle heterogeneity (Hosseini et al., 2020). To facilitate comparison to PKIKP studies, we convert the travel times of I2* to the single pass through the IC time equivalent dividing the residuals by two. (c) Stacks of coda-correlation waveforms per bin shown in (a). The *y*-axis indicates the coordinates of the center of each bin.

$$t_{I2^*} = \delta t_{obsI2^*} - \left(t_{ellipt} + t_{mantle}\right) \quad (2)$$

where δt_{obsI2^*} is the differential travel time between observed I2* and a reference waveform (obtained as the stack of all the equatorial paths only), and t_{ellipt} and t_{mantle} are the correction times for the Earth's ellipticity and mantle heterogeneities, respectively.

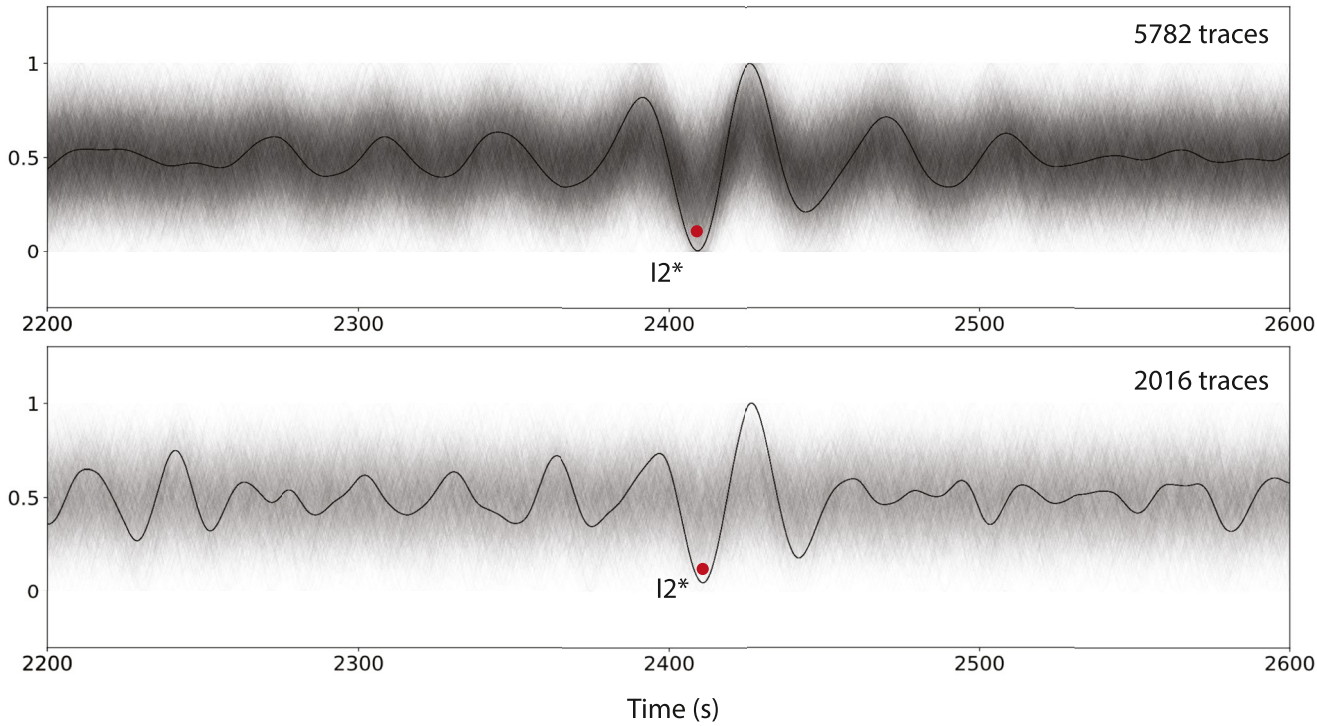

Figure 6. Individual cross-correlation functions ranging between 2,200 and 2,600 s after the correlation-origin time, and I2* waveforms sampling two different geographical bins (indicated in Figure 5). In each panel, thin waveforms are cross-correlation functions calculated for records of each station-pair from 4° to 9° inter-receiver distances. The total numbers of waveforms in each bin are indicated in the top right, and the thick waveforms are linear stacks. The top and bottom panel indicate the waveforms of the bin in latitude 15° and longitude 292.5°, and latitude 45° and longitude 112.5° (Figure 5c), respectively. I2* arrival is denoted by a red dot near 2,420 s.

3. Results

3.1. Cylindrical Anisotropy in the IC

Figure 5 shows the global distribution of I2* residuals sampling the IC and their corresponding stacked waveforms. The data points sampling moderate and low latitudes are more abundant than those sampling the core parallel to ERA. These quasi-polar directions ($\xi \leq 35°$) are poorly represented in differential PKP travel time studies. Large earthquakes mainly sample these directions from events in the South Sandwich Islands (SSI) recorded by stations in Alaska, and occasional northern latitude events recorded in Antarctica. The scarcity in azimuthal coverage of high-quality quasi-polar paths imposes a limitation on anisotropy investigations of the central part of the IC.

Conversely, I2* quasi-polar paths can be estimated from any records of high-latitude earthquakes recorded by any station pair deployed at short inter-receiver distances, adding to the antipodal source-station geometry. Also, distinct from PKPbc-PKIKP and PKPab-PKIKP differential travel times, the bottoming depth of our selected I2* in the IC does not depend on the epicenter distance: they sample the central part of the IC, with turning radii from about 80 to 170 km. Thus, our dataset uniquely provides information regarding the IMIC seismic properties.

We model IC anisotropy by first converting the travel times of I2* to the time equivalent to a single pass through the IC. We divide the residuals by two to facilitate comparison with models derived from PKIKP studies. Then, we estimate the uncertainty in the travel times and ξ* of raypaths caused by a biased sampling of the stacked waveforms. We use bootstrap resampling to evaluate the confidence intervals of the data, and we used these uncertainties as weight parameters in the least-square anisotropy modeling.

For a transversely isotropic medium, the seismic velocity of body waves depends on its propagation direction relative to the fast-axis. Residuals of compressional waves in the IC have been modeled using different models of cylindrical anisotropy (a type of transverse isotropy), including the parametrization of radial and azimuthal variations of anisotropy strength. Here, we estimate the parameters of a cylindrically anisotropic bulk IC with

constant anisotropy with depth, and we also model the IMIC after correcting for the OIC anisotropy. For cylindrical anisotropy, the P-wave velocity perturbation to an isotropic velocity can be expressed as a function of ξ, the angle of the raypath with the rotation axis as:

$$\frac{\delta v_p}{v_p} = \varepsilon \cos^2 \xi + \sigma \sin^2 \xi \cos^2 \xi + \gamma_0 \tag{3}$$

where ε and σ are parameters related to the Love's parameters (e.g., Ishii & Dziewoński, 2003; Morelli et al., 1986), and γ_0 is a baseline shift. The perturbation in the compressional wave speed $\delta v_p / v_p$ can be converted to the travel-time residuals δt by an integration of the velocity perturbation along the raypath s in the IC:

$$\delta t = -\int_s \frac{1}{v_p} \frac{\delta v_p}{v_p} ds \tag{4}$$

By combining Equations 3 and 4, we estimate the solutions ε, σ, and γ_0 of anisotropy using a weighted least-square method. We fit the observations to the model predictions of a bulk IC (Equation S1 in Supporting Information S1) and IMIC anisotropy (Equation S2 in Supporting Information S1). The misfit criteria are quantified by the variance $\mathrm{VR} = \left(\sum (\mathrm{obs} - \mathrm{pred})^2 / \sum (\mathrm{obs})^2\right)$, and $R^2 = 1 - \left(\sum \left(\mathrm{obs} - \mathrm{pred}\right)^2 / \sum \left(\mathrm{obs} - \overline{\mathrm{obs}}\right)^2\right)$, where $\overline{\mathrm{obs}}$ is the mean of the observations, displayed in Table S2 of Supporting Information S1.

Figure 7 shows the I2* time residuals as a function of ξ* and the comparison between our model and predictions of IC anisotropy proposed by several previous studies. After correcting the residuals for multiple models of mantle heterogeneities, we find the best fit for the bulk IC anisotropy with $\varepsilon = 0.020\ (\pm 0.003)$, $\sigma = -0.071\ (\pm 0.014)$, and $\gamma_0 = -0.019\ (\pm 0.004)$. Next, we correct the residuals for anisotropy in the OIC, and model the observation for the best fitting IMIC. We find an IMIC anisotropy with $\varepsilon_2 = 0.033\ (\pm 0.008)$, $\sigma_2 = -0.129\ (\pm 0.03)$, $\gamma_0 = -0.013\ (\pm 0.004)$, and a radius of 650 km fits the data equally well to a model of anisotropic bulk IC. We estimate the solutions of ε and σ parameters using a weighted least-square method (see Supporting Information S1 for an explanation of these parameters). The preferred IMIC model is chosen based on the R^2 and VR misfit (Table S2 in Supporting Information S1; OIC model of Stephenson et al., 2020) for several values of the IMIC radii. Notably, a prominent slower propagation of compressional waves near $\xi^* = 55°$ is observed consistently for all azimuths (red sectors in Figure 5). In the sections below, we provide a discussion of a possible origin of this pattern of residuals.

3.2. Uncertainty Estimation of the I2* Travel-Times and ξ*

The uncertainty in the travel-time observations and the angle ξ* of I2* raypaths is estimated via bootstrap resampling analysis. Firstly, we randomly resample the waveforms 1,000 times within each bin. For many uses, such as estimation of confidence intervals, calculating the average and standard deviation of 1,000 random resamples provides adequate approximations of statistical uncertainties (Hesterberg, 2011). This value represents a trade-off between computational expense and improved accuracy of estimation of confidence levels.

For the bth set of resamples, we obtain a bth stacked waveform and calculate its ξ* as the median. We then use cross-correlation to obtain the travel-time difference between the I2* waveform of the bth stacked trace and the reference waveform, where the reference waveform is the stacked cross-correlation function of the original set of waveforms. We allow for repetitions and variation in the size of samples for every degree of interstation distance. This provides 1,000 estimates of travel-time and angle, each utilizing a statistical resample of the data, representing the variation in our measurements given slightly different sampling geometries or data coverage. Our observed invariability of the I2* correlogram times and the angles ξ* in differently sampled data indicates that our observations are highly stable and insensitive to potential sampling variations in the input dataset (Table S3 in Supporting Information S1).

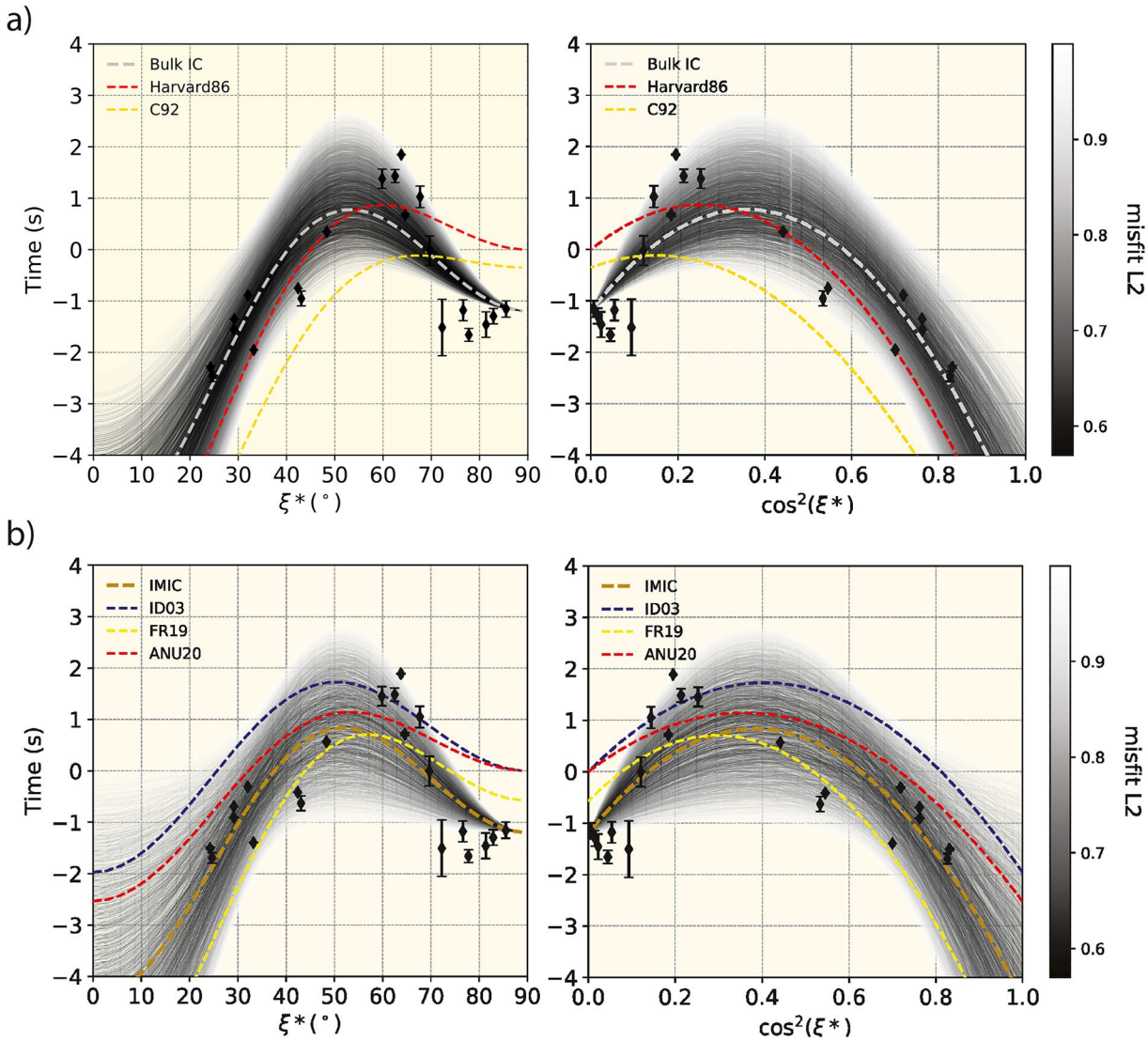

Figure 7. Modeling of IC cylindrical anisotropy and comparison with previously published models. (a) Travel-time residuals of I2* (diamonds) as a function of ξ^* (equivalent to the angle ξ used in PKP studies; panel to the left) and as a function of $\cos^2 \xi^*$(panel to the right). The error bars are 95% confidence intervals (too small to be seen along the x-axis). The uncertainty estimation is described in Table S3 of Supporting Information S1. The thick gray dashed curve is the optimal model of cylindrical anisotropy for the bulk IC obtained by the least-square method. The misfit is the normalized L2-norm between observation and prediction. Shades of gray show the ensemble of the 10% lowest misfit models according to the misfit bar shown on the right. Dashed curves in red, and yellow are the bulk IC cylindrical anisotropy models by Morelli et al. (1986), and Creager (1992). The travel time anomaly is related to the velocity perturbation along the 180° (antipodal) raypath for a source at the depth of 0 km (we consider the time of I2* in the IC equivalent to double the PKIKP time). (b) Travel-time residuals of I2* (diamonds) corrected for the OIC (the top 570 km of the IC) anisotropy model of Stephenson et al. (2020) as a function of ξ^* (panel to the left) and $\cos^2 \xi^*$(panel to the right). Note the two data points between 20 and 30° are shifted toward 0 by about 1 s in comparison with the data in (a). Dark yellow dashed curve is the optimal model of cylindrical anisotropy for the IMIC (the innermost 650 km of the IC) obtained by the least-square method. Shades of gray show the ensemble of the 10% lowest misfit models. Dashed curves in blue, yellow, and red are the IMIC cylindrical anisotropy models of Ishii and Dziewoński (2003), Frost and Romanowicz (2019), and Stephenson et al. (2020). For the ε_2, σ_2, $\gamma 0$, and IMIC radius information, see Supporting Information S1.

4. Discussion

We explore the medium-range period correlation feature I2* (15–50 s), whose constituents traverse the IC through its innermost part. For short inter-receiver distances, the I2*'s constituents' sample equal lengths through the OIC and IMIC and thus the travel time residuals of I2* we observe results from the wave propagation through both volumes of the IC. Although this trade-off limits our radial resolution of anisotropy and limits our ability to determine whether there is a sharp transition to the IMIC, we test the influence of the OIC by correcting the

travel times for multiple anisotropy models obtained from the selected PKP studies (Frost & Romanowicz, 2019; Ishii & Dziewoński, 2003; Stephenson et al., 2020). After the corrections, a highly prominent slow propagation is present at $\xi^* = 55°$ regardless of the OIC model, which has been observed for the IMIC but not for the OIC. Thus, we interpret that the prominent slow direction at $\xi^* = 55°$ that we observe stems from the IMIC, with an anisotropic structure fundamentally different from the OIC.

4.1. Implications for the IC Structure and Dynamics

The transition in the anisotropic pattern from the OIC to the IMIC is marked by a change in the direction of the slow axis of propagation, with a poor resolution on the exact radius where this occurs. A few geodynamical models have been proposed to explain the presence of a distinct anisotropy in the innermost region of the IC: (1) Diminishing strength of thermal convection over time (Cottaar & Buffett, 2012). Combined convective cooling episodes and compositional buoyancy could have occurred at the early stages of the IC growth and terminated before the present day. Consequently, a distinct anisotropy pattern would be expected in the portion of the IC subjected to convection, that is, the IMIC. (2) Preferential crystallization due to the transition in the deformation pattern over time coupled with density stratification (Deguen & Cardin, 2009). The variation of IC anisotropy with depth could be induced during IC solidification or post-solidification deformation regimes. In the model by Deguen and Cardin (2009), a strain variation over time was proposed as a mechanism in which the IC gradually evolves from a deformation regime penetrating the whole IC at early stages to confined to the upper part only; in other words, this dynamical model corresponds to multiple stages of different IC growth patterns resulting in radial transitions. Thus, the IMIC would represent a fossil anisotropy linked to Maxwell stresses recorded at the early stages of IC formation. (3) The IC's growth could have been conditioned by the sedimentation of light elements at the ICB, which is linked to chemical variations in the outer core (Alfè et al., 2002; Badro et al., 2007). In this scenario, the increase in light elements in the outer core as the IC solidified would generate radial transitions in density, and consequently different solidification and texturing patterns over time. The presence of the IMIC would thus represent a period of transition in the geodynamical and compositional properties of the IC (Labrosse, 2014).

4.2. Novelty and Limitations of This Study

I2* waveforms carry seismic information of the central part of the core, leading to an unprecedented volumetric coverage of the IMIC. Also, it overcomes the shortage of strictly antipodal source-receiver ray paths required in studies utilizing the direct wavefield. Because I2* is observed at cross-correlation functions of records at any pair of receivers deployed within near inter-receiver distances, it offers a new range of tools for the exploration of the Earth's deep interior. Its prominent expression in the coda correlograms facilitates the geometrical sampling of the IC in multiple directions. However, the sensitivity of its constituents to both OIC and IMIC structure also leads to uncertainties on the radial constraint of anisotropy. This uncertainty can be minimized when our results are complemented by data sensitive to the OIC used in PKP studies. Finally, the main disadvantage of our method is its computational cost. There is a significant amount of time associated with processing the waveforms and calculating the correlograms, and an extensive virtual space is required to store the data. Furthermore, the sampling coverage we propose depends on stacks of correlation functions in each bin, which can be uneven and lead to poorly sampled or empty bins.

4.3. A Tilt of the Symmetry Axis of Anisotropy

Different studies have investigated a possibility that the fast axis of IC cylindrical anisotropy (also its symmetry axis) could be misaligned with the ERA (e.g., Creager, 1992; Irving & Deuss, 2011; McSweeney et al., 1997; Souriau & Romanowicz, 1996; Su & Dziewonski, 1995). We conduct a grid search to estimate the optimal orientation of the symmetry axis using the equations of transverse isotropy (Equation 3). We measure the misfit between the observations and the theoretical prediction as we change the coordinates of the reference axis. For every change in the coordinate system, the angle ξ^* of all raypaths is recalculated, and the parameters of anisotropy are estimated using a weighted least square. The test of symmetry axis is performed by fitting the bulk IC, and also for the IC containing IMIC after various corrections of OIC anisotropy. Mathematically, both models

of bulk IC and IMIC result in nearly equal fit with the optimal symmetry axis near the north pole (Figure S6 in Supporting Information S1), located at 85°N and 10°E (±5°). However, we cannot establish that this result is significantly better than the fast axis aligned with ERA. Namely, the considerable uncertainty is due to the size of our bins and the long period nature of I2*.

4.4. Comparison Between Body-Wave and Coda-Correlation Studies

Tkalčić and Phạm (2018) directly compare the shear-waves velocity in the IC from models estimated by body waves, normal modes, and earthquake coda-correlation using the formulation of Dziewoński and Anderson (1981). Moreover, Ma and Tkalčić (2021) showed that the time difference between the seismic phases observed in models constructed by body-waves and the model constructed using the coda-correlation wavefield (CCREM) is small: that is, for I2*, the residual time is around 0.8 s between CCREM and ek137 or CCREM and ak135. In conclusion, the velocity variations for different periods (1, 15, and 50 s) are not significant.

Here, we compare our observations to recent and independent IC studies using body wave travel times. I2* time propagation in the IC is an integration over its entire depth, and the trade-off between anisotropy strength and IMIC radius imposes a limitation on the interpretation of anisotropy models: I2* lacks radial resolution because it is traverses both OIC and IMIC. We observe the slow direction of propagation near 55° from the ERA, which has not been detected by PKP data sensitive to the upper 600 km below ICB. Thus, when our observations are combined with the current constraints on the IC structure, there is a strong agreement between on the IMIC's slow direction and parameters of anisotropy. We interpret our observations as evidence for a distinct anisotropic structure in the innermost part of the IC.

Our findings support an anisotropic IMIC previously hypothesized based on the PKIKP travel time observations (Ishii & Dziewoński, 2002) and confirmed in subsequent studies (e.g., Beghein & Trampert, 2003; Cao & Romanowicz, 2007; Ishii & Dziewoński, 2003; Niu & Chen, 2008). Despite the model of IMIC proposed by these studies being inconsistent in regards to the radius of the IMIC and direction of the slow axis of anisotropy, their common denominator is that the innermost part of the IC shows a fundamentally different pattern of anisotropy from the bulk IC. Using a cylindrical model of anisotropy, our observations require a slow axis of propagation directed at $\xi = 55°$ from ERA. Our results agree with the most recent model of Stephenson et al. (2020), which characterized the IMIC as a significant change in the strength of the slow axis of anisotropy (a pronounced negative σ parameter), rather than defining its properties according to the fast direction.

Additionally, our observations provide further support for a fast axis of anisotropy in the IMIC oriented near the polar direction, from a distinct and different type of data. This is in contrast to the IMIC structure proposed by T. Wang et al. (2015) and T. Wang and Song (2018). In these studies, the authors use autocorrelation to "extract body wave signals" and investigate IC anisotropy through the principle of Green's function's reconstruction (i.e., assumption that I2* is equivalent to the I2), suggesting a fast axis of anisotropy aligned in the equatorial plane. However, due to the time errors associated with the seismic propagation of the I2* constituents (as shown by Tkalčić et al., 2020; S. Wang & Tkalčić, 2020a, 2020b), the utilization of Green's functions leads to a misinterpretation of anisotropy in the IC (Figure S4 in Supporting Information S1). Here, we carefully select the constituents of I2* by utilizing the podal-antipodal source-receiver configuration; the energy distribution of I2* is confined to the great circle plane, where the energy of strong reverberation is dominant (Sens-Schönfelder et al., 2015). Consequently, we suppress the travel time influence of the I2* cross-terms raised by stations deployed away from the stationary point (i.e., the point of the same slowness for the I2* constituents; S. Wang & Tkalčić, 2020a). The source-receiver geometry then satisfies the stationary phase principle, and the ray theory can approximately predict the timing of I2*.

The lack of evidence for a fast anisotropy axis in the equatorial direction in the IMIC was also corroborated in PKIKP studies of Romanowicz et al. (2016) and Frost and Romanowicz (2019). Most recently, Frost et al. (2021) have proposed a single geodynamic model of IC evolution that fits multiple seismic observations coupled with parameters of outer core dynamics and mineral phase predictions. Their findings are based on PKIKP travel-time analysis and indicate the anisotropy in the IC is stronger with depth and offset from ERA. Significantly, their study also shows no evidence for a fast equatorial anisotropy in the IMIC. Despite a different resolution band of our dataset, our studies converge in concluding that the fast anisotropy axis in the IMIC is in the polar, not the equatorial direction.

5. Conclusions

We present a new method based on the correlation wavefield, which enables retrieval of IC-sensitive signals from the records of large events' late-coda cross-correlation. Unlike the PKIKP travel-time studies based on the antipodal configuration of sources and receivers, our method benefits from the many station pairs deployed in small inter-receiver distances. We use time measurements of I2*, a correlation feature sensitive to the whole IC, including its innermost 600 km. Given that I2*'s formation depends on the source-receiver geometry, we use this as a guiding principle for our strict selection of podal-antipodal source-station orientation. The choice of the optimal location of the earthquakes and receivers before calculating the cross-correlations and stacking is crucial to avoid unwanted constituents biasing the I2* correlogram times.

A model of IMIC anisotropy with the following parameters: $\sigma = -12.9\%$ and $\varepsilon = 3.3\%$, can optimally fit our observations. Our results indicate that the cylindrical anisotropy strength has a pronounced dip ∼55° from ERA, agreeing with the most recent robust parameter search using PKIKP travel times (Stephenson et al., 2020). Interestingly, the difference between the slow (the cube's side) and the fast (the cube's main diagonal) axes in the bcc iron is 54.73° (Belonoshko et al., 2008, 2021), while pure hcp iron ranges between 40° and 55° in previous studies (e.g., Romanowicz et al., 2016; Vočadlo et al., 2009). This match might suggest that the IMIC consists of either a set of oriented bcc or hcp crystals. Recently, S. Wang and Tkalčić (2021) observed IC anisotropy in shear through the analysis of the correlation feature I2–J. They demonstrated that, while the bcc001 structure could be ruled out, the other two bcc structures and hcp are not distinguishable.

The travel-time variation of I2* favors a faster P-wave propagation along the polar direction than along the equator, which agrees with other IMIC studies using body-wave travel times (e.g., Frost & Romanowicz, 2019; Ishii & Dziewoński, 2002; Romanowicz et al., 2016). We furthermore show that a potential tilt of the symmetry axis of anisotropy by 5° (85°N and 10°E) from ERA fits the observed data reasonably well. However, our resolution is limited by the long-period nature of our dataset, and we cannot establish it as a significantly better solution than the ERA-aligned anisotropy.

Although our data do not allow us to resolve the radius of the IMIC, we conclude that our observations are consistent with a distinct anisotropy in the deepest part of the IC. The transition from OIC to IMIC possibly signifies a dynamic event from the early stage of IC formation. Multiple correlation features emerging in the coda-correlation wavefield provide opportunities for investigations of the Earth's deep interior. Undoubtedly, the development of alternative seismological tools is at the forefront of efforts to overcome the limitation of the IC volumetric sampling, and improve our understanding of its structure and evolution.

Acknowledgments
The waveforms used in this study were downloaded from IRIS-DMC and processed on the computing facilities at the Research School of Earth Sciences (RSES), the Australian National University. Synthetic calculations were performed on the Terrawulf cluster, a computational facility supported through the AuScope initiative. AuScope Ltd. is funded under the National Collaborative Research Infrastructure Strategy (NCRIS), an Australian Commonwealth Government Programme. The authors are grateful to the Global Seismology group members at the RSES, in particular to Thanh-Son Phạm, Sheng Wang and Xiaolong Ma for their significant contributions to the current understanding of the nature of the coda-correlation wavefield. The authors also acknowledge comments and suggestions from Daniel A. Frost and an anonymous reviewer that improved the original version of the manuscript. T. Costa de Lima is grateful to Thanh-Son Phạm for providing his code for the global cross-correlation computation. L. Waszek's time at RSES was supported by the Australian Research Council's Discovery Early Career Research Award DE170100329. Open access publishing facilitated by Australian National University, as part of the Wiley - Australian National University agreement via the Council of Australian University Librarians.

Data Availability Statement

Raw seismic data are downloaded from Incorporated Research Institution for Seismology Data Management Center (IRIS DMC, https://ds.iris.edu/ds/nodes/dmc/) using ObsPy software package (Beyreuther et al., 2010). The information of 105 events and stations used in this study is available at https://figshare.com/articles/dataset/Events-stations_zip/19069463. All the figures are made with Matplotlib (Hunter, 2007).

References

Alfè, D., Gillan, M. J., & Price, G. D. (2002). Ab initio chemical potentials of solid and liquids solutions and the chemistry of the Earth's core. *The Journal of Chemical Physics*, *116*(16), 7127–7136. https://doi.org/10.1063/1.1464121

Badro, J., Fiquet, G., Guyot, F., Gregoryanz, E., Occelli, F., Antonangeli, D., & d'Astuto, M. (2007). Effect of light elements on the sound velocities in solid iron: Implications for the composition of Earth's core. *Earth and Planetary Science Letters*, *254*(1–2), 233–238. https://doi.org/10.1016/j.epsl.2006.11.025

Beghein, C., & Trampert, J. (2003). Robust normal mode constraints on inner-core anisotropy from model space search. *Science*, *299*(5606), 552–555. https://doi.org/10.1126/science.1078159

Belonoshko, A. B., Fu, J., & Smirnov, G. (2021). Free energies of iron phases at high pressure and temperature: Molecular dynamics study. *Physical Review B*, *104*(10). https://doi.org/10.1103/PhysRevB.104.104103

Belonoshko, A. B., Skorodumova, N. V., Rosengren, A., & Johansson, B. (2008). Elastic anisotropy of Earth's inner core. *Science*, *319*(5864), 797–800. https://doi.org/10.1126/science.1150302

Bensen, G. D., Ritzwoller, M. H., & Shapiro, N. M. (2008). Broadband ambient noise surface wave tomography across the United States. *Journal of Geophysical Research*, *113*(5). https://doi.org/10.1029/2007JB005248

Bergman, M. I. (1997). Erratum: Measurements of elastic anisotropy due to solidification texturing and the implications for the Earth's inner core. *Nature*, *389*(6649), 412. https://doi.org/10.1038/38786

Bergman, M. I., Yu, J., Lewis, D. J., & Parker, G. K. (2018). Grain boundary sliding in high-temperature deformation of directionally solidified hcp Zn alloys and implications for the deformation mechanism of Earth's inner core. *Journal of Geophysical Research: Solid Earth*, *123*(1), 189–203. https://doi.org/10.1002/2017JB014881

Beyreuther, M., Barsch, R., Krischer, L., Megies, T., Behr, Y., & Wassermann, J. (2010). ObsPy: A python toolbox for seismology. *Seismological Research Letters*, *81*(3), 530–533. https://doi.org/10.1785/gssrl.81.3.530

Boué, P., Poli, P., Campillo, M., Pedersen, H., Briand, X., & Roux, P. (2013). Teleseismic correlations of ambient seismic noise for deep global imaging of the Earth. *Geophysical Journal International*, *194*(2), 844–848. https://doi.org/10.1093/gji/ggt160

Boué, P., Poli, P., Campillo, M., & Roux, P. (2014). Reverberations, coda waves and ambient noise: Correlations at the global scale and retrieval of the deep phases. *Earth and Planetary Science Letters*, *391*, 137–145. https://doi.org/10.1016/j.epsl.2014.01.047

Buffett, B. A., Huppert, H. E., Lister, J. R., & Woods, A. W. (1992). Analytical model for solidification of the Earth's core. *Nature*, *356*(6367), 329–331. https://doi.org/10.1038/356329a0

Calvet, M., Chevrot, S., & Souriau, A. (2006). P-wave propagation in transversely isotropic media. II. Application to inner core anisotropy: Effects of data averaging, parametrization and a priori information. *Physics of the Earth and Planetary Interiors*, *156*(1–2), 21–40. https://doi.org/10.1016/j.pepi.2006.01.008

Campillo, M., & Paul, A. (2003). Long range correlations in the diffuse seismic coda. *Science*, *299*(5606), 547–549. https://doi.org/10.1126/science.1078551

Cao, A., & Romanowicz, B. (2007). Test of the innermost inner core models using broadband PKIKP travel time residuals. *Geophysical Research Letters*, *34*. https://doi.org/10.1029/2007GL029384

Cormier, V. F., & Stroujkova, A. (2005). Waveform search for the innermost inner core. *Earth and Planetary Science Letters*, *236*(1–2), 96–105. https://doi.org/10.1016/j.epsl.2005.05.016

Cottaar, S., & Buffett, B. (2012). Convection in the Earth's inner core. *Physics of the Earth and Planetary Interiors*, *198–199*, 67–78. https://doi.org/10.1016/j.pepi.2012.03.008

Creager, K. C. (1992). Anisotropy of the inner core from differential travel times of the phases PKP and PKIKP. *Nature*, *356*(6367), 309–314. https://doi.org/10.1038/356309a0

Deguen, R., & Cardin, P. (2009). Tectonic history of the Earths inner core preserved in its seismic structure. *Nature Geoscience*, *2*(6), 419–422. https://doi.org/10.1038/ngeo522

Dziewoński, A. M., & Anderson, D. L. (1981). Preliminary reference Earth model. *Physics of the Earth and Planetary Interiors*, *25*(4), 297–356. https://doi.org/10.1016/0031-9201(81)90046-7

Ekström, G., Nettles, M., & Dziewoński, A. M. (2012). The global CMT project 2004–2010: Centroid-moment tensors for 13,017 earthquakes. *Physics of the Earth and Planetary Interiors*, *200–201*, 1–9. https://doi.org/10.1016/j.pepi.2012.04.002

Feng, J., Yao, H., Poli, P., Fang, L., Wu, Y., & Zhang, P. (2017). Depth variations of 410 km and 660 km discontinuities in eastern North China Craton revealed by ambient noise interferometry. *Geophysical Research Letters*, *44*, 8328–8335. https://doi.org/10.1002/2017GL074263

Frost, D. A., Lasbleis, M., Chandler, B., & Romanowicz, B. (2021). Dynamic history of the inner core constrained by seismic anisotropy. *Nature Geoscience*, *14*, 531–535. https://doi.org/10.1038/s41561-021-00761-w

Frost, D. A., & Romanowicz, B. (2019). On the orientation of the fast and slow directions of anisotropy in the deep inner core. *Physics of the Earth and Planetary Interiors*, *286*, 101–110. https://doi.org/10.1016/j.pepi.2018.11.006

Gubbins, D., Alfè, D., Masters, G., Price, G. D., & Gillan, M. J. (2003). Can the Earth's dynamo run on heat alone? *Geophysical Journal International*, *155*(2), 609–622. https://doi.org/10.1046/j.1365-246X.2003.02064.x

Hesterberg, T. (2011). Bootstrap. *Wiley Interdisciplinary Reviews: Computational Statistics*, *3*(6), 497–526. https://doi.org/10.1002/wics.182

Hosseini, K., Sigloch, K., Tsekhmistrenko, M., Zaheri, A., Nissen-Meyer, T., & Igel, H. (2020). Global mantle structure from multifrequency tomography using P, PP and P-diffracted waves. *Geophysical Journal International*, *220*(1), 96–141. https://doi.org/10.1093/gji/ggz394

Huang, H. H., Lin, F. C., Tsai, V. C., & Koper, K. D. (2015). High-resolution probing of inner core structure with seismic interferometry. *Geophysical Research Letters*, *42*(24), 10622–10630. https://doi.org/10.1002/2015GL066390

Hunter, J. D. (2007). Matplotlib: A 2D graphics environment. *Computing in Science & Engineering*, *9*(3), 90–95. https://doi.org/10.1109/MCSE.2007.55

Irving, J. C. E., & Deuss, A. (2011). Hemispherical structure in inner core velocity anisotropy. *Journal of Geophysical Research: Solid Earth*, *116*(4). https://doi.org/10.1029/2010JB007942

Ishii, M., & Dziewoński, A. M. (2002). The innermost inner core of the Earth: Evidence for a change in anisotropic behavior at the radius of about 300 km. *Proceedings of the National Academy of Sciences of the United States of America*, *99*(22), 14026–14030. https://doi.org/10.1073/pnas.172508499

Ishii, M., & Dziewoński, A. M. (2003). Distinct seismic anisotropy at the centre of the Earth. *Physics of the Earth and Planetary Interiors*, *140*(1–3), 203–217. https://doi.org/10.1016/j.pepi.2003.07.015

Jackson, I., Fitz Gerald, J. D., & Kokkkkonen, H. (2000). High-temperature viscoelastic relaxation in iron and its implications for the shear modulus and attenuation of the Earth's inner core. *Journal of Geophysical Research: Solid Earth*, *105*(B10), 23605–23634. https://doi.org/10.1029/2000jb900131

Jacobs, J. A. (1953). The Earth's inner core. *Nature*, *172*(4372), 297–298. https://doi.org/10.1038/172297a0

Jeanloz, R., & Wenk, H.-R. (1988). Convection and anisotropy of the inner core. *Geophysical Research Letters*, *15*(1), 72–75. https://doi.org/10.1029/GL015i001p00072

Karato, S. I. (1993). Inner core anisotropy due to the magnetic field-induced preferred orientation of iron. *Science*, *262*(5140), 1708–1711. https://doi.org/10.1126/science.262.5140.1708

Karato, S. I. (1999). Seismic anisotropy of the Earth's inner core resulting from flow induced by Maxwell stresses. *Nature*, *402*(6764), 871–873. https://doi.org/10.1038/47235

Kennett, B. L. N., Engdahl, E. R., & Buland, R. (1995). Constraints on seismic velocities in the Earth from traveltimes. *Geophysical Journal International*, *122*(1), 108–124. https://doi.org/10.1111/j.1365-246X.1995.tb03540.x

Kennett, B. L. N., & Gudmundsson, O. (1996). Ellipticity corrections for seismic phases. *Geophysical Journal International*, *127*(1), 40–48. https://doi.org/10.1111/j.1365-246X.1996.tb01533.x

Kennett, B. L. N., & Phạm, T. S. (2018a). The nature of Earth's correlation wavefield: Late coda of large earthquakes. *Proceedings of the Royal Society A: Mathematical, Physical & Engineering Sciences*, *474*(2214), 20180082. https://doi.org/10.1098/rspa.2018.0082

Kennett, B. L. N., & Phạm, T. S. (2018b). Evolution of the correlation wavefield extracted from seismic event coda. *Physics of the Earth and Planetary Interiors*, *282*, 100–109. https://doi.org/10.1016/j.pepi.2018.07.004

Labrosse, S. (2014). Thermal and compositional stratification of the inner core. *Comptes Rendus Geoscience*, *346*(5–6), 119–129. https://doi.org/10.1016/j.crte.2014.04.005

Labrosse, S., & Macouin, M. (2003). The inner core and the geodynamo. *Comptes Rendus Geoscience*, *335*(1), 37–50. https://doi.org/10.1016/S1631-0713(03)00013-0

Lehmann, I. (1936). P', publ. *Bureau Central Séismologique International. Serie A*, *14*, 87–115.

Li, Y., Vočadlo, L., & Brodholt, J. P. (2018). The elastic properties of hcp-Fe alloys under the conditions of the Earth's inner core. *Earth and Planetary Science Letters*, *493*, 118–127. https://doi.org/10.1016/j.epsl.2018.04.013

Lin, F. C., & Tsai, V. C. (2013). Seismic interferometry with antipodal station pairs. *Geophysical Research Letters*, *40*, 4609–4613. https://doi.org/10.1002/grl.50907

Loper, D. E. (1984). Structure of the core and lower mantle. *Advances in Geophysics*, *26*(C), 1–34. https://doi.org/10.1016/S0065-2687(08)60243-5

Ma, X., & Tkalčić, H. (2021). CCREM: New reference Earth model from the global coda-correlation wavefield. *Journal of Geophysical Research: Solid Earth*, *126*(9), e2021JB022515. https://doi.org/10.1029/2021JB022515

Mattesini, M., Belonoshko, A. B., & Tkalčić, H. (2018). Polymorphic nature of iron and degree of lattice preferred orientation beneath the Earth's inner core boundary. *Geochemistry, Geophysics, Geosystems*, *19*(1), 292–304. https://doi.org/10.1002/2017GC007285

McSweeney, T. J., Creager, K. C., & Merrill, R. T. (1997). Depth extent of inner-core seismic anisotropy and implications for geomagnetism. *Physics of the Earth and Planetary Interiors*, *101*(1–2), 131–156. https://doi.org/10.1016/S0031-9201(96)03216-5

Morelli, A., Dziewoński, A. M., & Woodhouse, J. H. (1986). Anisotropy of the inner core inferred from PKIKP travel times. *Geophysical Research Letters*, *13*(13), 1545–1548. https://doi.org/10.1029/GL013i013p01545

Nissen-Meyer, T., Van Driel, M., Stähler, S. C., Hosseini, K., Hempel, S., Auer, L., et al. (2014). AxiSEM: Broadband 3-D seismic wavefields in axisymmetric media. *Solid Earth*, *5*(1), 425–445. https://doi.org/10.5194/se-5-425-2014

Niu, F., & Chen, Q. F. (2008). Seismic evidence for distinct anisotropy in the innermost inner core. *Nature Geoscience*, *1*(10), 692–696. https://doi.org/10.1038/ngeo314

Phạm, T. S., & Tkalčić, H. (2018). Antarctic ice properties revealed from teleseismic P wave coda autocorrelation. *Journal of Geophysical Research: Solid Earth*, *123*(9), 7896–7912. https://doi.org/10.1029/2018JB016115

Phạm, T. S., Tkalčić, H., Sambridge, M., & Kennett, B. L. N. (2018). Earth's correlation wavefield: Late coda correlation. *Geophysical Research Letters*, *45*(7), 3035–3042. https://doi.org/10.1002/2018GL077244

Poli, P., Campillo, M., & de Hoop, M. (2017). Analysis of intermediate period correlations of coda from deep earthquakes. *Earth and Planetary Science Letters*, *477*, 147–155. https://doi.org/10.1016/j.epsl.2017.08.026

Poli, P., Campillo, M., & Pedersen, H. (2012). Body-wave imaging of Earth's mantle discontinuities from ambient seismic noise. *Science*, *338*(6110), 1063–1065. https://doi.org/10.1126/science.1228194

Poli, P., Thomas, C., Campillo, M., & Pedersen, H. A. (2015). Imaging the D″ reflector with noise correlations. *Geophysical Research Letters*, *42*(1), 60–65. https://doi.org/10.1002/2014GL062198

Poupinet, G., Pillet, R., & Souriau, A. (1983). Possible heterogeneity of the Earth's core deduced from PKIKP travel times. *Nature*, *305*(5931), 204–206. https://doi.org/10.1038/305204a0

Retailleau, L., Boué, P., Li, L., & Campillo, M. (2020). Ambient seismic noise imaging of the lowermost mantle beneath the North Atlantic Ocean. *Geophysical Journal International*, *222*, 1339–1351. https://doi.org/10.1093/gji/ggaa210

Ritterbex, S., & Tsuchiya, T. (2020). Viscosity of hcp iron at Earth's inner core conditions from density functional theory. *Scientific Reports*, *10*(1). https://doi.org/10.1038/s41598-020-63166-6

Romanowicz, B., Cao, A., Godwal, B., Wenk, R., Ventosa, S., & Jeanloz, R. (2016). Seismic anisotropy in the Earth's innermost inner core: Testing structural models against mineral physics predictions. *Geophysical Research Letters*, *43*(1), 93–100. https://doi.org/10.1002/2015GL066734

Ruigrok, E., Draganov, D., & Wapenaar, K. (2008). Global-scale seismic interferometry: Theory and numerical examples. *Geophysical Prospecting*, *56*(3), 395–417. https://doi.org/10.1111/j.1365-2478.2008.00697.x

Sabra, K. G., Gerstoft, P., Roux, P., Kuperman, W. A., & Fehler, M. C. (2005). Extracting time-domain Green's function estimates from ambient seismic noise. *Geophysical Research Letters*, *32*(3), 1–5. https://doi.org/10.1029/2004GL021862

Sens-Schönfelder, C., Snieder, R., & Stähler, S. C. (2015). The lack of equipartitioning in global body wave coda. *Geophysical Research Letters*, *42*(18), 7483–7489. https://doi.org/10.1002/2015GL065108

Shapiro, N. M., & Campillo, M. (2004). Emergence of broadband Rayleigh waves from correlations of the ambient seismic noise. *Geophysical Research Letters*, *31*(7), a–n. https://doi.org/10.1029/2004GL019491

Snieder, R., Wapenaar, K., & Larner, K. (2006). Spurious multiples in seismic interferometry of primaries. *Geophysics*, *71*(4), SI111–SI124. https://doi.org/10.1190/1.2211507

Souriau, A., & Romanowicz, B. (1996). Anisotropy in inner core attenuation: A new type of data to constrain the nature of the solid core. *Geophysical Research Letters*, *23*(1), 1–4. https://doi.org/10.1029/95GL03583

Stephenson, J., Tkalčić, H., & Sambridge, M. (2020). Evidence for the innermost inner core: Robust parameter search for radially varying anisotropy using the neighbourhood algorithm. *Journal of Geophysical Research: Solid Earth*, *126*(1), e2020JB020545. https://doi.org/10.1029/2020JB020545

Stixrude, L., & Cohen, R. E. (1995). High-pressure elasticity of iron and anisotropy of Earth's inner core. *Science*, *267*(5206), 1972–1975. https://doi.org/10.1126/science.267.5206.1972

Su, W.-J., & Dziewonski, A. M. (1995). Inner core anisotropy in three dimensions. *Journal of Geophysical Research*, *100*(B6), 9831–9852. https://doi.org/10.1029/95JB00746

Tkalčić, H. (2017). *The Earth's inner core: Revealed by observational Seismology*. Cambridge University Press. https://doi.org/10.1017/9781139583954

Tkalčić, H., Flanagan, M. P., & Cormier, V. F. (2006). Observation of near-podal P′P′ precursors: Evidence for back scattering from the 150–220 km zone in the Earth's upper mantle. *Geophysical Research Letters*, *33*(3). https://doi.org/10.1029/2005GL024626

Tkalčić, H., & Phạm, T. S. (2018). Shear properties of Earth's inner core constrained by a detection of J waves in global correlation wavefield. *Science*, *362*(6412), 329–332. https://doi.org/10.1126/science.aau7649

Tkalčić, H., & Phạm, T.-S. (2020). Excitation of the global correlation wavefield by large earthquakes. *Geophysical Journal International*, *223*(3), 1769–1779. https://doi.org/10.1093/gji/ggaa369

Tkalčić, H., Phạm, T. S., & Wang, S. (2020). The Earth's coda correlation wavefield: Rise of the new paradigm and recent advances. *Earth-Science Reviews*, *208*, 103285. https://doi.org/10.1016/j.earscirev.2020.103285

Tromp, J. (1993). Support for anisotropy of the Earth's inner core from free oscillations. *Nature*, *366*(6456), 678–681. https://doi.org/10.1038/366678a0

Van Driel, M., & Nissen-Meyer, T. (2014). Seismic wave propagation in fully anisotropic axisymmetric media. *Geophysical Journal International*, *199*(2), 880–893. https://doi.org/10.1093/gji/ggu269

Vinnik, L., Romanowicz, B., & Breger, L. (1994). Anisotropy in the center of the inner core. *Geophysical Research Letters*, *21*(16), 1671–1674. https://doi.org/10.1029/94GL01600

Vočadlo, L., Dobson, D. P., & Wood, I. G. (2009). Ab initio calculations of the elasticity of hcp-Fe as a function of temperature at inner-core pressure. *Earth and Planetary Science Letters*, *288*(3–4), 534–538. https://doi.org/10.1016/j.epsl.2009.10.015

Wang, S., & Tkalčić, H. (2020a). Seismic event coda-correlation's formation: Implications for global seismology. *Geophysical Journal International*, *222*(2), 1283–1294. https://doi.org/10.1093/gji/ggaa259

Wang, S., & Tkalčić, H. (2020b). Seismic event coda-correlation: Toward global coda-correlation tomography. *Journal of Geophysical Research: Solid Earth*, *125*(4). https://doi.org/10.1029/2019jb018848

Wang, S., & Tkalčić, H. (2021). Shear-wave anisotropy in the Earth's inner core. *Geophysical Research Letters*, *48*. https://doi.org/10.1029/2021gl094784. e2021GL0974784

Wang, T., & Song, X. (2018). Support for equatorial anisotropy of Earth's inner-inner core from seismic interferometry at low latitudes. *Physics of the Earth and Planetary Interiors*, *276*, 247–257. https://doi.org/10.1016/j.pepi.2017.03.004

Wang, T., Song, X., & Xia, H. H. (2015). Equatorial anisotropy in the inner part of Earth's inner core from autocorrelation of earthquake coda. *Nature Geoscience*, *8*(3), 224–227. https://doi.org/10.1038/ngeo2354

Wapenaar, K., Draganov, D., Snieder, R., Campman, X., & Verdel, A. (2010). Tutorial on seismic interferometry: Part 1—Basic principles and applications. *Geophysics*, *75*(5), 75A195–75A209. https://doi.org/10.1190/1.3457445

Wapenaar, K., & Fokkema, J. (2006). Green's function representations for seismic interferometry. *Geophysics*, *71*(4), SI33–SI46. https://doi.org/10.1190/1.2213955

Woodhouse, J. H., Giardini, D., & Li, X.-D. (1986). Evidence for inner core anisotropy from free oscillations. *Geophysical Research Letters*, *13*(13), 1549–1552. https://doi.org/10.1029/GL013i013p01549

Wu, B., Xia, H. H., Wang, T., & Shi, X. (2018). Simulation of core phases from coda interferometry. *Journal of Geophysical Research: Solid Earth*, *123*(6), 4983–4999. https://doi.org/10.1029/2017JB015405

Xia, H. H., Song, X., & Wang, T. (2016). Extraction of triplicated PKP phases from noise correlations. *Geophysical Journal International*, *205*(1), 499–508. https://doi.org/10.1093/gji/ggw015

Yoshida, S., Sumita, I., & Kumazawa, M. (1996). Growth model of the inner core coupled with the outer core dynamics and the resulting elastic anisotropy. *Journal of Geophysical Research B: Solid Earth*, *101*(12), 28085–28103. https://doi.org/10.1029/96jb02700

Zhan, Z., Ni, S., Helmberger, D. V., & Clayton, R. W. (2010). Retrieval of Moho-reflected shear wave arrivals from ambient seismic noise. *Geophysical Journal International*, *182*(1), 408. https://doi.org/10.1111/j.1365-246X.2010.04625.x